INL/EXT-16-40010 Rev. 0

September 2016

Overview of lower length scale model development for accident tolerant fuels regarding U_3Si_2 fuel and FeCrAl cladding

Yongfeng Zhang
Daniel Schwen
Larry Aagesen
Karim Ahmed
Jianguo Yu
Benjamin Beeler
Chao Jiang

David Andersson

INL/EXT-16-40010 Rev. 0

Overview of lower length scale model development for accident tolerant fuels regarding U_3Si_2 fuel and FeCrAl cladding

Yongfeng Zhang
Daniel Schwen
Larry Aagesen
Karim Ahmed
Jianguo Yu
Benjamin Beeler
Chao Jiang

*David Andersson**

September 2016

Idaho National Laboratory
Fuel Modeling and Simulation Department
Idaho Falls, Idaho 83415

***Los Alamos National Laboratory**

Prepared for the
U.S. Department of Energy
Office of Nuclear Energy
Under U.S. Department of Energy-Idaho Operations Office
Contract DE-AC07-99ID13727

ABSTRACT

U_3Si_2 and FeCrAl have been proposed as fuel and cladding concepts, respectively, for accident tolerance fuels with higher tolerance to accident scenarios compared to UO_2. However, a lot of key physics and material properties regarding their in-pile performance are yet to be explored. To accelerate the understanding and reduce the cost of experimental studies, multiscale modeling and simulation are used to develop physics-based materials models to assist engineering scale fuel performance modeling. In this report, the lower-length-scale efforts in method and material model development supported by the Accident Tolerance Fuel (ATF) high-impact-problem (HIP) under the NEAMS program are summarized. Significant progresses have been made regarding interatomic potential, phase field models for phase decomposition and gas bubble formation, and thermal conductivity for U_3Si_2 fuel, and precipitation in FeCrAl cladding. The accomplishments are very useful by providing atomistic and mesoscale tools, improving the current understanding, and delivering engineering scale models for these two ATF concepts.

CONTENTS

FIGURES

1 Introduction

Following the Fukushima Daiichi accident in 2011, the development of accident tolerant fuels (ATFs) has become a primary direction in nuclear fuel research and development for light water reactors (LWRs) [1]. Compared with the standard oxide fuel (UO_2 fuel with Zr-alloy cladding), the ATFs - including both fuels and claddings - are required to have better or at least comparable performance during normal operation, and better performance at accident scenarios such as loss of coolant accident (LOCA). The ATFs are expected to sustain a longer time than the oxide fuel under off-normal conditions and thus allows for enhanced safety margins. Two leading concepts, triuraniumdisilicide (U_3Si_2) as fuel and FeCrAl as cladding respectively, have attracted wide research and applied interests.

U_3Si_2 has higher thermal conductivity than that of UO_2 at operating temperatures, resulting in lower fuel centerline temperatures. It also has a higher U density, which may enable some new cladding concepts that would otherwise require increased enrichment limits to compensate for their neutronic penalty. Compared to the Zr-alloy claddings, FeCrAl alloys have superior resistance to water corrosion (oxidation) and higher mechanical strength at high temperatures [2]. The good corrosion resistance reduces the heat and hydrogen generation produced by reaction with coolant during severe accidents. The high mechanic strength enhances the burst margin of the cladding. The good corrosion resistance comes from the high Cr concentration and the formation of an aluminum-oxide layer at the surface.

To utilize U_3Si_2 and FeCrAl in realistic fuels, the primary challenge is that their in-pile and out-of-pile behaviors have not been extensively tested for fuel safety and reliability. Meanwhile, the current understanding from material science point of view is far from sufficient to develop a theoretical prediction of their performance. To accelerate the understanding and to reduce the cost of experimental studies, multiscale modeling and simulations in analogy to that for UO_2 fuel are utilized to improve the fundamental understanding and to develop materials models. Moreover, for U_3Si_2 and FeCrAl, tools required for studies at the atomistic scale and mesoscale are yet to be developed. In FY16, lower-length-scale efforts have been made to develop the needed tools at various scales and to develop engineering scale materials models for certain properties, targeting a long-term objective of replicating the success on UO_2 fuel achieved under the NEAMS program.

In this report, the progresses made in FY16 are summarized with proper amount of technical details. For some topics, a separate report will be created with rich details. In these cases, brief summary will be provided by citing the more detailed reports. A research plan for FY17 will also be provided in the Summary Section.

2 Interatomic potential for U_3Si_2

In order to perform engineering scale nuclear fuel performance simulations, the material properties of the fuel must be known. Currently, the experimental data available for U-Si fuels is rather limited. Thus, multiscale modeling efforts are underway to address this gap in knowledge. First principles calculations have been carried out characterizing a variety of properties in the USi system [3]. These calculations have provided insight where experimental information is lacking. However these types of simulations are limited in their ability to investigate properties at finite temperatures and in their ability to investigate systems above a few hundred atoms. Unlike most first principles calculations, interatomic potentials based on mostly classical descriptions can be used to calculate relevant atomistic properties above 0 K and up to millions of atoms. Semi-empirical interatomic potentials can be fitted to both first principles and experimental data and employed to simulate high temperature properties. In classical simulations atoms are represented by point-like centers, which interact through many-body interactions defined by a set of equations-the interatomic potential. In that way the highly complex description of electron dynamics investigated in first principles calculations is replaced by an effective model whose main features such as the hard core of particles and internal degrees of freedom are described by a set of parameters and analytical functions, which depend on the mutual positions of the atoms in the configuration. These parameters and functions give complete information about the system energy, as well as about the forces acting on each particle. Utilizing interatomic potentials in molecular statics and dynamics simulations, information can be obtained on a nanometer and nanosecond scale that can then be input into higher level modeling software such as phase field. Very few interatomic potentials have been constructed for either metallic uranium or uranium-based alloys, and no such potentials for the U-Si system have been constructed prior to this work. In FY16, two interatomic potentials, one Tersoff type and one modified Embedded-Atom Method (MEAM) type, are developed for U_3Si_2 and summarized below. These two potentials will be further evaluated and they are expected to have good performance on different properties.

2.1 Tersoff type potential

The details of the Tersoff type potential for U-Si have been described in previous publications and report [4, 5]. Here only brief introduction will be given. To fit an interatomic potential, a suitable formalism needs to be decided considering the bonding nature in the material system and the material properties of interest. For instance, in freshly fabricated U_3Si_2 fuels there are usually secondary phases such as U_3Si and/or USi. Furthermore, silicide compounds (U_3Si_2 and U_3Si) are known to become amorphous under irradiation at low temperatures. Based on the above considerations, the Tersoff type bond-order formalism is selected as it can treat both metallic and covalent bonding. A Tersoff type Si potential existing in the literature has been shown to describe liquid and amorphous Si phases well, as well as other crystallographic phases of Si. Therefore, this Si potential is used here to describe the Si-Si interaction in U-Si systems. However, so far there have been no Tersoff type U potentials that can describe all possible U phases, α, β, and γ. To come up with a U-Si potential, we start with the development of a Tersoff type U potential. Based on the existing Si and the U potential developed here, cross-term parameters for U-Si interactions are fitted for binary U-Si phases including U_3Si_2 and U_3Si. During the fitting, we focus on the U_3Si_2 phase, which is the primary fuel candidate of our accident tolerant fuel high-impact-problem (ATF-HIP) project.

The development is based on the Tersoff type potentials for single element U and Si. The Si potential is taken from the literature and a Tersoff type U potential is developed in this project.

With the primary focus on the U_3Si_2 phase, some other U-Si systems such as U_3Si are also included as a test of the transferability of the potentials for binary U-Si phases. In summary, based on the potentials for unary U and Si, two sets of parameters are obtained for U-Si systems using cross-term fitting (the cross-term potential) and the Tersoff mixing rules (the Tersoff mixing potential), respectively. Data from experiments and DFT calculations are used to fit and to assess the fitting results. While both potentials show satisfactory fitting results on the lattice constants and enthalpies of formations for U_3Si_2 and U_3Si phases, the cross-term potential is found to be superior to the Tersoff mixing potential in all areas. The former also produces much better agreement with the literature data on the elastic constants of U_3Si_2. Therefore, the cross-term potential is likely to be the choice for possible further improvement and may probably be used to study mechanical properties with/without irradiation as well.

The unary U potential developed here serves as the basis to obtain a U-Si potential, which is the primary focus. It reasonably reproduces the literature data on the lattice constants and cohesive energies of (α, β, γ)-U phases, showing some transferability of the potential. However, it fails to predict the right phase order between βU and γU with a negligible energetic difference between them. Therefore, it would e hard for this potential to distinguish these two phases at finite temperatures. However, it's not clear if any phase transition will happen if a simulation starts with one of these two phases.

In order to tackle the fission gas formation and its impact on fuel swelling and to provide useful parameters using MD simulations for mesoscale models in MARMOT to study radiation damage, fission gas, interfaces and the interactions between them, we have also been developing potential parameters for Xe in U-Si system. In particular, there are 6 interactions in Xe-U-Si ternary potential. So far, the potential parameters available are: the interaction of Si-Si taken from the literature and the interactions of U-U and U-Si developed above. Thus three more interactions are needed: Xe-Xe, U-Xe, and Si-Xe.

Based on the literature review of Xe potentials with transport properties, two types of existed Xe potentials (Lennard-Jones [LJ] potential and Hartree-Fock-Dispersion-B [HFD-B] potential) are selected as the baseline to fit two Tersoff potentials. LJ potential can describe Xe transport properties very well in low temperature range, but over underestimates that at high temperatures due to overestimated short-range repulsive part. HFD-B potential is reasonable at low temperatures and very good at high temperatures. We found that the developed two Tersoff potentials for Xe reproduce the corresponding potential in the potential zone ($2.5 < r < 5\mathring{A}$) very well. In the short-range repulsive zone for $r < 2.5\mathring{A}$ and in the long-range attractive zone for $r > 5\mathring{A}$, the developed two Tersoff potentials have almost identical potential energy surface (PES), which is very similar with HFD-B potential. It seems that both LJ based Tersoff Xe potential and HFD-B based potential will describe transport properties for Xe well, but LJ based is better at low temperatures. Meanwhile, we fitted the interactions of Si-Xe and obtained a parameter set predicting the results for the potential energy as a function of distance, agreeing well with the DFT dataset.

Having developed 5 interactions in Xe-U-Si ternary potential, future plans include development of a reasonable parameter set for the interactions of U-Xe which can predict the results for the potential energy as a function of distance in good agreement with the DFT dataset. Using the fully parameterized potential, MD simulations will be carried out to study the fission gas formation and its impact on fuel swelling, and interfacial energies in order to provide useful parameters for meso-scale MARMOT simulations.

2.2 MEAM type potential

2.2.1 MEAM Theory

The Embedded-Atom Method (EAM) [6, 7, 8] has been shown to predict the properties of alloys and metals quite well. The EAM is the most widely used semi-empirical potential, with applications including calculations of point defects [9], melting [10], grain boundary structure and energy [11], dislocations [12] [40], segregation [13], fracture [14] and surface structure [15]. The basis of the EAM is that the cohesive energy can be expressed in terms of embedding energies. In this view, each atom in the metal is embedded into the electron gas created by the other atoms. The EAM provides a robust means of calculating structure and energetics; however, it is best suited strictly for purely metallic systems with no directional bonding. From the EAM, the total energy of a system of atoms is given by equation 2.2.1.

$$E = \sum_i \{F(\bar{\rho}_i) \ + \frac{1}{2}\sum_{j \neq i} \phi(R_{ij})\} \tag{1}$$

where i and j are the individual atoms of the model [8, 6]. The pair interaction between atoms i and j is given by ϕ [16] and is dependent on the separation between the atoms Rij.

$$\phi(R) = \frac{2}{Z}\{E^u(R) - F(\frac{\bar{\rho}^0(R)}{Z})\} \tag{2}$$

In equation 2.2.1, Z is the number of first neighbors, $\bar{\rho}^0(R)$ is the background electron density and $\{E^u(R)$ is the per atom energy of the reference structure as a function of nearest-neighbor distance R [17] obtained from the universal equation of state of Rose et al. [15] given in equation 2.2.1.

$$E^u(R) = -E_c(1 + a^* + \delta \times (\frac{r_e}{r}) \times (a^*)^3)e^{(-a^*)} \tag{3}$$

with

$$a^* = \alpha(\frac{R}{r_e} - 1) \tag{4}$$

and

$$\alpha^2 = \frac{9\omega B}{E_c} \tag{5}$$

where E_c, r_e, ω and B are the cohesive energy, nearest neighbor distance, atomic volume and bulk modulus, respectively, evaluated at equilibrium in the reference structure. In this work, the reference structure is taken as face-centered cubic, resulting in:

$$\bar{\rho}^0(R) = Z\rho^{a(0)}(R) \tag{6}$$

where $\rho^{a(0)}$ is an atomic electron density discussed below. The embedding function, F, is given in equation 2.2.1 and is the energy required to embed atom i into a system with a background electron density $\bar{\rho}_i$.

$$F(\bar{\rho}) = AE_c\frac{\bar{\rho}}{z}ln\frac{\bar{\rho}}{z} \tag{7}$$

For this work, Z=ρ_0=12. The modification to the EAM is a function of how the electron density at a certain point, ρ_i, is calculated. In the traditional EAM, ρ_i is simply the linear supposition of spherically averaged atomic electron densities:

$$\rho_i^{(0)} = \sum_{j\neq i}\rho_j^{a(0)}(R_{ij}) \tag{8}$$

whereas the MEAM introduces angularly dependent terms to augment $\bar{\rho}_i$ as shown in equations 2.2.1 through equation 2.2.1 [17, 18].

$$(\rho_i^{(1)})^2 = \sum_{\alpha}\{\sum_{j\neq i}x_{ij}^{\alpha}\rho_i^{a(1)}(R_{ij})\}^2 = \sum_{j,k\neq i}\rho_j^{a(1)}(R_{ij})\rho_k^{a(1)}(R_{ik})cos\{\theta_{ijk}\} \tag{9}$$

$$(\rho_i^{(2)})^2 = \sum_{\alpha,\beta}\{\sum_{j\neq i}x_{ij}^{\alpha}x_{ij}^{\beta}\rho_j^{a(2)}(R_{ij})\}^2 - \frac{1}{3}\sum_{j\neq i}[\rho_j^{a(2)}(R_{ij})]^2 \tag{10}$$

$$(\rho_i^{(3)})^2 = \sum_{\alpha,\beta,\gamma}\{\sum_{j\neq i}x_{ij}^{\alpha}x_{ij}^{\beta}x_{ij}^{\gamma}\rho_j^{a(3)}(R_{ij})\}^2 - \frac{3}{5}\sum_{j\neq i}[\rho_j^{a(3)}(R_{ij})]^2 \tag{11}$$

Here, the $\rho^{a(l)}$ are the atomic densities which represent the decrease in the contribution with distance R_{ij} and the α, β, γ summations are each over the three coordinate directions with x_{ij}^{α} being the distance the ratio R_{ij}^{α}/R_{ij} with R_{ij}^{α} being the α component of the distance vector between atoms i and j [29]. Similar to equation 2.2.1, equations 2.2.1 and 2.2.1 can be put in a form that has a dependence on the angle between atoms i,j and k (θ_{ijk}), and this has been done by Baskes et al. [19]. Atomic electron densities are assumed to decrease exponentially,

$$\rho_i^{a(l)}(R) = e^{[-\beta^{(l)}(\frac{R}{r_e}-1)]} \tag{12}$$

where $\beta^{(l)}$ are the decay lengths. To obtain the background electron density from the partial electron densities we make the assumption that the angular terms are a small correction to the EAM.

$$(\rho_i^{(0)})^2 = \sum_{l=0}^{3}t_i^{(l)}(\rho_i^{(l)})^2 \tag{13}$$

Many body screening is implemented through a screening function, S_{ik}, that quantifies screening between two atoms i and k due to other atoms in the system, j. The atomic electron densities and the pair potential are multiplied by this function. The screening function depends on all other atoms in the system:

$$S_{ijk} = \Pi_{j\neq i,k}S_{ijk} \tag{14}$$

where S_{ijk} is calculated using a simple geometric construction. The screening factor S_{ijk} is defined as:

$$S_{ijk} = f_c[\frac{c - c_{min}}{c_{max} - c_{min}}] \tag{15}$$

Where C is a geometric parameter, and C_{min} and C_{max} are limiting values of C. The smooth cutoff function is:

$$f_c(x) = \begin{cases} 1 & x \geq 1 \\ [1 - (1-x)^6]^2 & 0 < x < 1 \\ 0 & x \leq 0 \end{cases} \tag{16}$$

A radial cutoff function is also applied to the atomic electron densities and pair potential which is given by $f_c[(r_c - r)/\lambda]$ where r_c is the cutoff distance of 6 and λ gives the cutoff region and was chosen to be 0.1. The MEAM has been shown to accurately predict the behavior of complex systems such as plutonium [17] and tin [20].

2.2.2 Fitting Procedure

In order to create a functional uranium-silicide (U-Si) binary interatomic potential, there must first exist (or be generated) suitable potentials for each individual element. A uranium potential from Moore, et. al [21] is utilized in the fitting. This MEAM interatomic potential performs excellently in describing the body-centered cubic phase of uranium and the alloy behavior of UZr. For the Si MEAM contribution, the initial potential utilized was from Baskes [16]. Upon finding this potential over-predicted the Si-Si dimer distance, the fitting of a new Si-Si potential was undertaken in an attempt to rectify this discrepancy, as well as increasing the vacancy formation energy in diamond cubic silicon. The resulting potential is shown in table 1, with the associated properties of the original and new MEAM potentials shown in table 2. The energy of the dimer was greatly increased, however the Si-Si distance is much closer to that of the predicted value of 2.17 Å. The formation energy of a vacancy in diamond Si is increased. All other properties are relatively unaffected.

The fitting procedure to develop cross-species parameters involves a starting guess, and is then refined via a script that gives a random step to all relevant fitting parameters. This updated potential is then input into LAMMPS [22] and a series of simulations are performed, the output of which is utilized to calculate a weighted-error summation. The script then either accepts or declines the prescribed changes to the fitting parameters based on the reduction of the total weighted-error. The emphasis of the fitting procedure was the U_3Si_2 phase, where cohesive energy, lattice constants and elastic constants were given priority with respect to the error weighting. A variety of other simulations were performed to fine-tune the potential, the entirety of which is beyond the scope of this report. Further refinement of the potential is ongoing, however, the fitting procedure was successful and produced a proficient potential. The potential parameters are shown in table 3.

For the sake of clarity and reproducibility, LAMMPS MEAM-specific parameters are included in table 4.

Table 1: Silicon MEAM potential parameters

Parameter	Original Si-MEAM	New Si-MEAM
alpha	4.87	4.87
b0	4.4	4.4662
b1	8.5	9.4016
b2	12.5	13.3826
b3	8.5	8.6993
alat	5.431	5.431
esub	4.63	4.63
asub	1	1
t0	1	1
t1	2.05	2.8841
t2	4.47	4.47
t3	-1.80	-1.80
Cmin	2.0	1.7215
Cmax	2.8	2.4942

Table 2: Properties of Silicon MEAM potentials. Units are as follows: E (ev/atom), a (Å), c_{xx} (GPa), E_{form} (eV).

Structure	Property	Original Si-MEAM	New Si-MEAM
Diamond	E	-4.63	-4.63
	a	5.431	5.431
	c_{11}	163.8	165.2
	c_{12}	64.6	64.6
	c_{44}	78.8	95.2
	E^{vac}_{form}	3.858	4.142
FCC	E	-4.065	-4.151
	a	4.100	4.098
HCP	E	-4.067	-4.152
	a	2.904	2.902
	c/a	1.624	1.624
SC	E	-4.337	-4.358
	a	2.622	2.622
BCC	E	-4.316	-4.286
	a	3.145	3.176
Dimer	E	-2.558	6.871
	a	2.431	2.095

Table 3: Uranium-Silicon MEAM potential parameters

Parameter	USi-MEAM
attrac	-0.1322
repuls	0.0046
alpha(1,2)	5.379
Cmin(2,2,1)	1.169
Cmax(2,2,1)	1.88
rho(2)	2.3843
rho(1)	1
Cmin(1,1,2)	0.221
Cmax(1,1,2)	2.386
Cmin(1,2,1)	2.021
Cmax(1,2,1)	2.795
Cmin(1,2,2)	1.464
Cmax(1,2,2)	2.407
Ec	5.36
re	3.05
lattce	l12

Table 4: LAMMPS MEAM-specific parameters

Parameter	USi-MEAM
bkgd_dyn	1
nn	1
delr	0.1
ialloy	1
augt1	0
emb_lin_neg	1

2.2.3 USi MEAM Potential Results

The results for basic fundamental properties of U_3Si_2 at 0 K are displayed in table 5 and compared to DFT calculations [3]. The formation energy is slightly overestimated, but the volume per atom and lattice constants are very accurate. The elastic constants show varying degrees of agreement with DFT predictions. Excellent agreement shown for C11, C22, C44 and C55, but significant variance is observed for C12 and C13, for example. The resulting bulk modulus (calculated via the elastic constants) is slightly overestimated.

Table 5: Properties of U_3Si_2 at 0 K. Results from the MEAM U-Si potential are compared to DFT calculations in REF.3.

	DFT	USi-MEAM
E	-0.364	-0.311
V/at	20.954	20.918
a	7.33	7.332
c	3.9	3.891
c/a	0.532	0.531
C11	158	160.3
C22	154	160.4
C33	140	121.7
C12	42	100.3
C13	46	104.8
C23	50	105.0
C44	66	61.4
C55	66	61.4
C66	45	21.5
B	81	118
G'xy	57	30
G'yz	49	18
G'xz	52	18

The U_3Si_2 structure as predicted by the MEAM potential is shown in figures 1 and 2, compared to the experimental structure. These figures denote a supercell of 2x2x2 unit cells with periodic boundaries. In figure 1, it is observed the presence of a slight deviation on the uranium atoms (red) in the mixed U-Si plane. At temperature, these uranium atoms exist above and below the mixed plane, with the average location of the uranium atoms equal to the experimental structure. In figure 2, it can be observed a minuscule rotation of atoms in the unit cell.

Point defect energies for the U_3Si_2 system are shown in table 6. Excellent general agreement is observed across all investigated defects, including both types of uranium vacancies, the silicon vacancies, all three types of anti-site defects, as well as bound and unbound Schottky defects.

In order to ensure that the potential is not restricted to studying only the U_3Si_2 phase, other phases, experimental and theoretical, were examined that were not included in the fitting procedure. These include FeB-USi, B1-USi, AlB2-USi_2, $L1_2$-USi_3, U_3Si_5 and the $L1_2$, alpha and beta phases of U_3Si. Summary charts of the results are shown in figures 3 and 4 as the formation energy as a function of uranium concentration and the volume per atom as a function of uranium concentration, respectively. In figure 3, there exists a general trend in that the formation energy predicted via

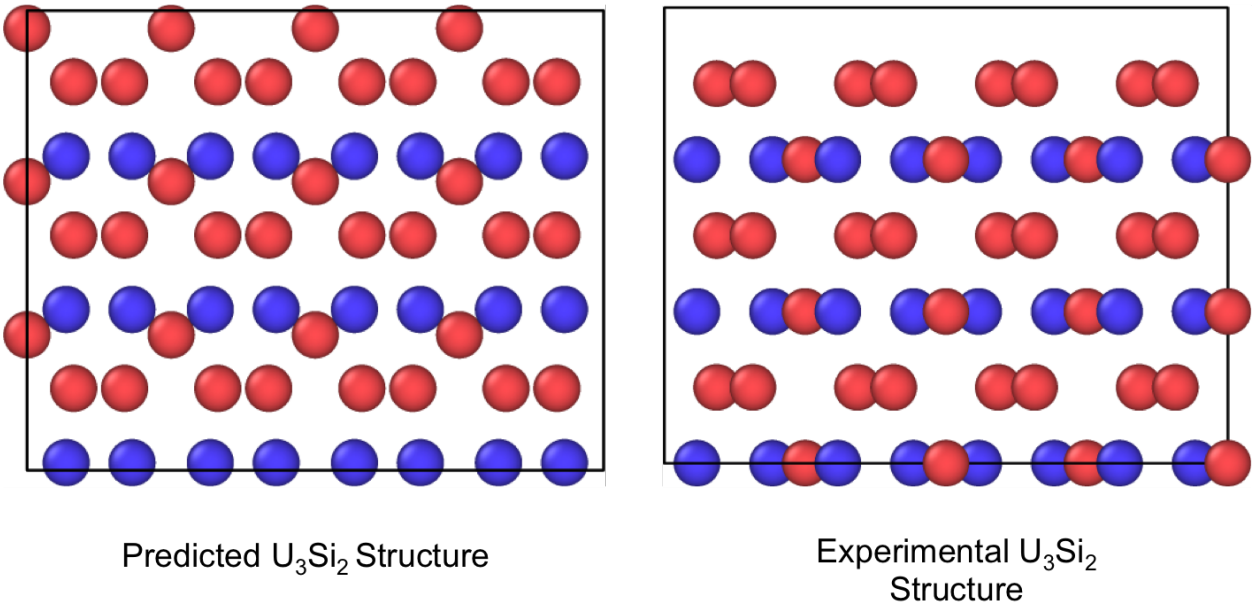

Figure 1: Predicted structure of U_3Si_2, (100) view.

Table 6: Properties of point defects in U_3Si_2 at 0 K. Results from the MEAM U-Si potential are compared to DFT calculations in REF.3.

	DFT	USi-MEAM
U vac 1	1.45	1.35
U vac 2	2.25	2.4
Si vac	1.14	1.86
U anti 1	0.79	0.81
U anti 2	2.19	1.73
Si anti	1.23	1.04
Schottky Unbound	9.90	10.37
Schottky Bound	7.67	7.71

the USi MEAM potential is generally higher compared to DFT. However, the general trends versus composition are excellent, with the only outlier being the $L1_2$-USi_3. In figure 4, there exists a trend in that the volume predicted via the USi MEAM potential is generally higher compared to DFT. The trends as a function of composition is not as accurate compared to the formation energy trends. The volume decrease on a phase change from the U_3Si_2 phase to the FeB-USi is not captured, as both phases have approximately the same volume per atom. However, given the overall trends across the variety of phases in the USi system that were not included into the fitting procedure, excellent agreement is observed.

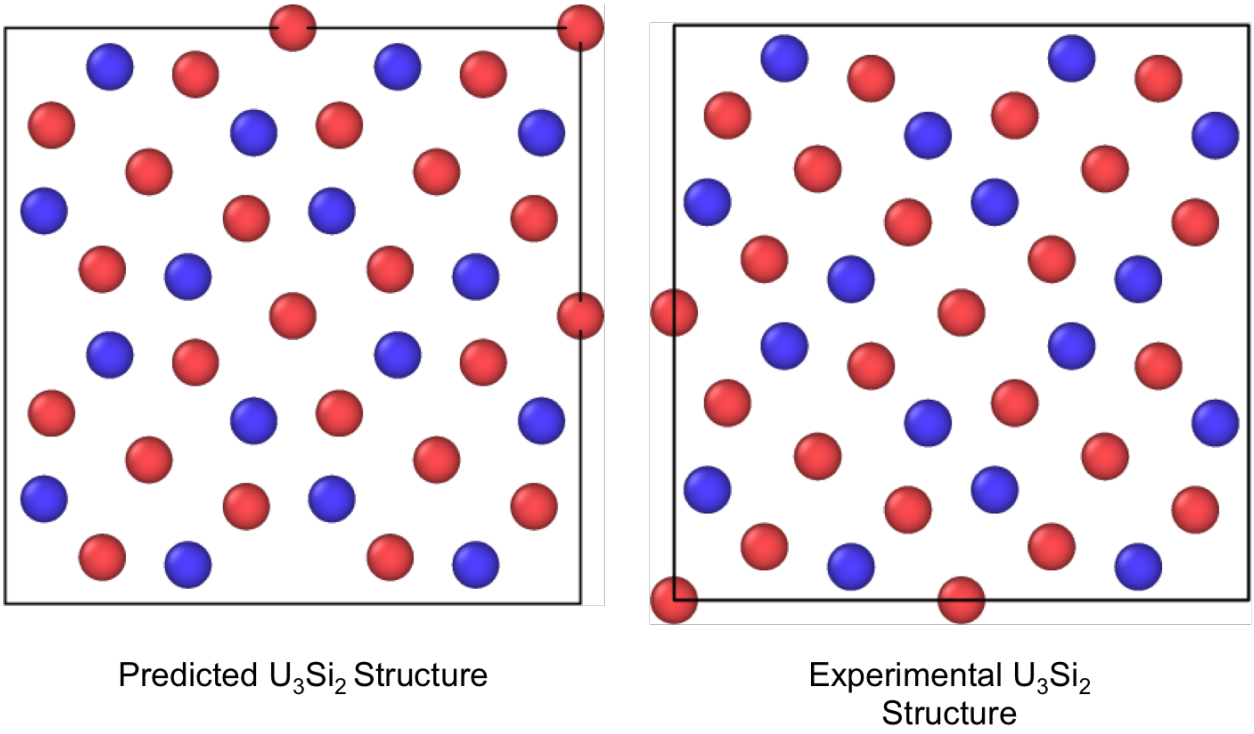

Figure 2: Predicted structure of U_3Si_2, (001) view.

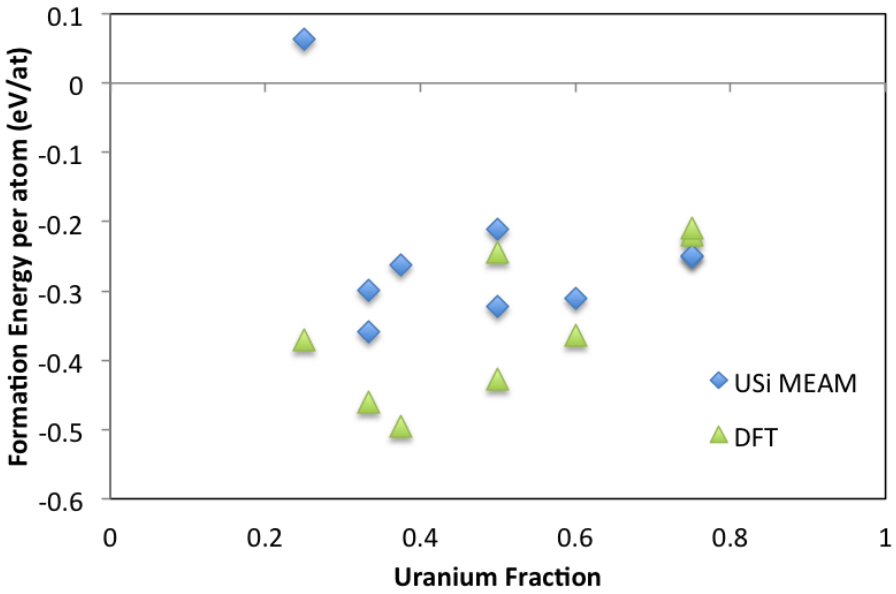

Figure 3: Formation energy per atom as a function of uranium concentration for a variety of phases in the USi system compared to DFT calculations in REF.3.

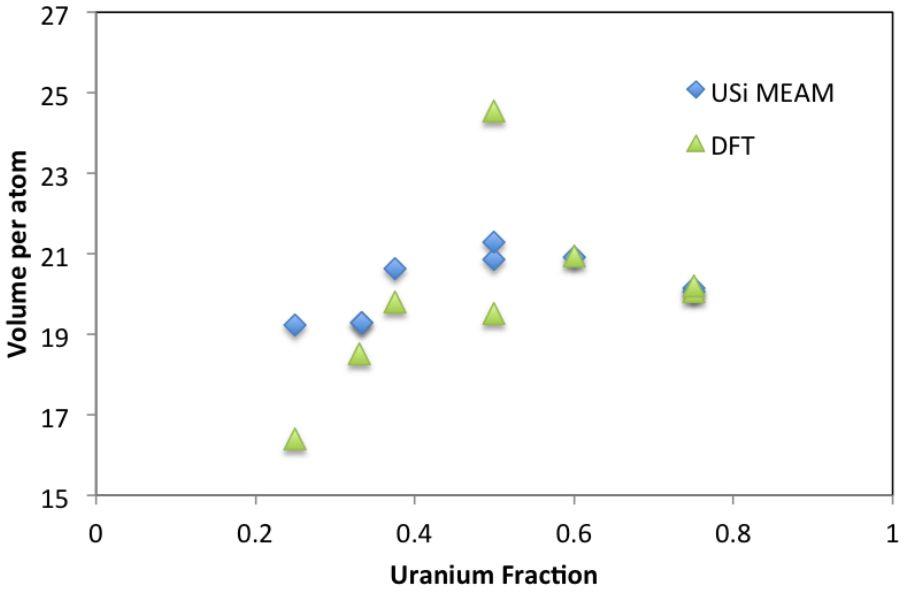

Figure 4: Volume per atom as a function of uranium concentration for a variety of phases in the USi system compared to DFT calculations in REF.3.

2.2.4 USi MEAM Summary

A MEAM interatomic potential was developed for the U-Si system. The potential accurately describes 0 K properties of the primary phase of interest (U_3Si_2), including formation energy, lattice constants, elastic constants and a variety of point defect properties. The potential can also reasonably predict properties of a variety of U-Si phases across the composition spectrum. This potential will be expanded to: 1) investigate a variety of thermodynamic properties at non-zero temperatures, 2) incorporate xenon for the study of fission gas behavior, 3) investigate grain boundaries and surfaces for implementation into phase-field models.

3 Phase field model development for phase stability of U-Si compounds

The U-Si system is under investigation for accident-tolerant fuel applications. Although multiple phases within this system have been investigated for use as nuclear fuel, U_3Si_2 has been found to be the most promising phase, because of its high U density, high thermal conductivity, and lower swelling with irradiation compared with other phases. To better understand the evolution of microstructure in U_3Si_2 during processing and in accident scenarios, a phase field model of the U-Si system has been developed in MARMOT.

The microstructure of U_3Si_2 usually contains inclusions of either the USi or U_3Si phases. Thus, the free energies of the U_3Si_2, USi, U_3Si, and liquid phases have been implemented in MARMOT based on a thermodynamic assessment conducted using the CALPHAD formalism. To investigate the evolution of microstructure during solidification processing or under conditions where melting could potentially occur, three phases need to be included (U_3Si_2, liquid, and USi or U_3Si).

A disadvantage of many existing phase-field models for three or more phases is that they allow spurious formation of additional phases at a two-phase interface, resulting in nucleation of new phases in unphysical locations and distorting the interfacial energies. Thus, a new three-phase model was developed and implemented in the MOOSE phase-field module based on the concepts of the (two-phase) Kim-Kim-Suzuki model. The behavior of this model was tested with both with a simplified system three-phase and the U-Si system. The model correctly reproduced three-phase coexistence in a U_3Si_2-liquid-USi system at the eutectic temperature, solidification of a three-phase mixture below the eutectic temperature, and complete melting of a three-phase mixture above the eutectic temperature. Further details are available in Ref. [23].

Having validated the three-phase KKS model and U-Si energies, future plans include implementation of unequal interfacial energies in the three-phase KKS model. This will require the addition of an additional kernel in the MOOSE phase-field module. Using data from lower length scale calculations, interfacial energies can be calculated and used as input to the phase-field model. Using the fully parameterized model, the behavior of U_3Si_2 fuel in accident scenarios will be investigated by imposing a temperature profile experienced in accident conditions and determining when liquid formation occurs for different microstructures.

4 Phase field model development for gas bubble swelling

The U-Si is under investigation as a candidate for accident-tolerant fuel applications. It has high U density and hence low fuel enrichment is required, which makes it attractive for non proliferation purposes. It also has a high thermal conductivity which is a crucial factor for accident-tolerant fuels. However, swelling rates in such metallic fuel are considerably higher than in uranium dioxide [24]. Therefore, investigating the process of fission gas segregation and subsequent bubble formation and growth in U-Si fuels is important for paving the way for the safe use of this fuel in commercial reactors.

A novel grand-potential phase field model for bubble formation and growth in U-Si fuels were developed. In contrast to the regular phase field models, the grand-potential formulation has the advantage of decoupling the interfacial and bulk properties. This facilitates specifying interfacial properties such as the interface width independently from the bulk properties, which enhances the computational efficiency. Furthermore, it can handle the numerical issue of very low defect concentrations that usually appear in irradiation effects problems since the primary variable is the chemical potential and not concentration as will be discussed below.

The grand-potential phase field model can be summarized as follows [25]. Instead of starting from a free energy functional as in the regular phase field models, one starts from a grand-potential functional as

$$\Omega(\mu,\phi) = \int h(\phi)\omega_b(\mu) + [1-h(\phi)]\omega_m(\mu) + g_{dw}(\phi) + \kappa|\nabla\phi|^2. \tag{17}$$

In the above, μ is the chemical potential, ϕ is the phase field that distinguishes between the bubble phase and the matrix (U-Si) phase, Ω is the total grand-potential, $h(\phi)$ is a smooth interpolation function with the value of 1.0 in the bubble phase and 0 in the matrix phase, ω_b is the bubble phase grand-potential, ω_m is the matrix phase grand-potential, $g_{dw}(\phi)$ is the regular double-well potential, κ is the gradient energy coefficient. The grand potential of a phase can be directly calculated from its free energy according to the thermodynamic relation $\omega_\alpha = f_\alpha(c) - \mu c$, where f is the free energy and c is the concentration. Note that the relation between the chemical potential and concentration must be invertible, so that the grand potential can be expressed in terms of the chemical potential.

The evolution equations are then developed by following the regular approach of irreversible thermodynamics. The phase field evolves according to the regular Allen-Cahn equation, e.g.,

$$\partial_t\phi = -L[h'(\phi)(\omega_b - \omega_m) + g'(\phi) - \kappa\nabla^2\phi], \tag{18}$$

where the prime means derivative with respect to the phase field. The evolution equation for the chemical potential can be derived from the balance law of the diffusing species c and it has the form,

$$\chi(\phi,\mu)\partial_t\mu = \nabla\cdot D(\phi,\mu)\chi(\phi,\mu)\nabla\mu - (c_b - c_m)g'(\phi)\partial_t\phi. \tag{19}$$

In this modified diffusion equation, D is the diffusion coefficient, $\chi = 1/\partial_c\mu$ is the susceptibility, and c_b and c_m are the equilibrium concentrations of the diffusing species in the bubble and matrix phases, respectively.

For our investigation of bubble formation and growth in U-Si, we consider the diffusion of of Xe gas atoms and vacancies. Therefore, two modified diffusion equations are coupled to the phase field equation and solved simultaneously. The model has been implemented in MARMOT. Two

new kernels called Susceptibility Time Derivative and Coupled Susceptibility Time Derivative that represent the products of a generalized susceptibility with the variables were added to MARMOT to allow solving the modified diffusion equation for different systems. For simplicity, we used parabolic free energy functions for the phases and hence the grand potentials of the phases are simply given by

$$\omega_m(\phi,\mu) = -\frac{\mu_g^2}{2A_g} - \mu_g c_g^{eq} - \frac{\mu_v^2}{2A_v} - \mu_v c_v^{eq}, \tag{20}$$

where v stands for vacancies and g for gas atoms, c_α^{eq} is the equilibrium value of the vacancy/gas atom concentration in the matrix, and $A_\alpha = \frac{\Omega_a}{c_\alpha^{eq} k_B T}$, with Ω_a being the atomic volume, k_B Boltzmann constant and T the absolute temperature. The equilibrium site fractions of Xe gas atoms and vacancies in the bubble are assumed to be 0.7 and 0.3, respectively.

An example of bubble growth in U_3Si_2 is considered here for illustrating the model capability. The formation and migration energies of vacancies and Xe atoms were taken from recent DFT calculations. The U_3Si_2 matrix is assumed to be initially supersaturated with vacancies and gas atoms (e.g., $c_v = c_g = 10^{-7}$). A snapshot showing the Xe atom concentration is shown in Fig.4. The evolution of the bubble radius with time at a temperature of 1200K is presented in Fig.4.

A few important model enhancements are required and will be added in future work. The polycrystalline nature of the U-Si matrix will be considered to simulate heterogeneous bubble nucleation and intergranular bubble growth. Also the resolution of gas bubbles will be modeled to capture accurately the bubble coarsening rate and hence the fuel swelling rate.

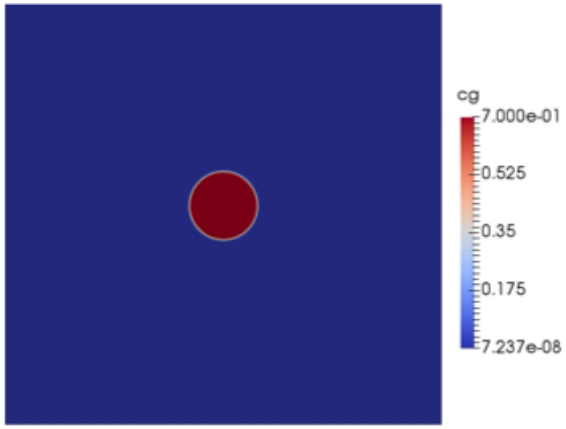

Figure 5: A snapshot showing the Xe gas atom concentration during bubble growth.

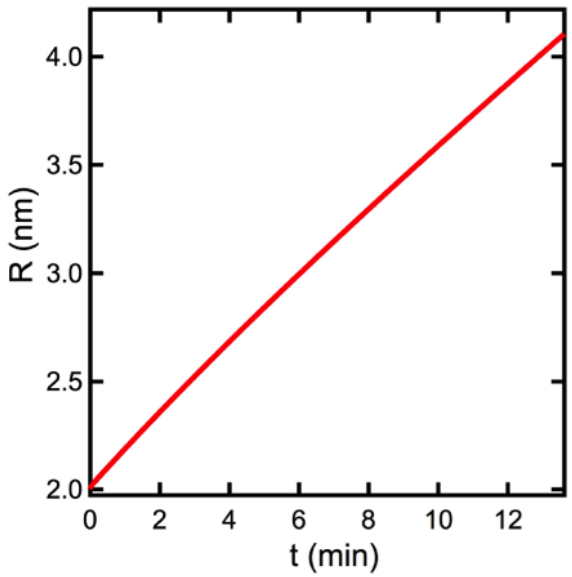

Figure 6: The evolution of the radius of Xe gas bubble from a supersaturated U_3Si_2 matrix at 1200K.

5 Thermal conductivity model development for U_3Si_2

As a leading ATF concept, the most appealing property of U_3Si_2 is its higher thermal conductivity than that of UO_2. More interestingly, its thermal conductivity increases with increasing temperature, in contrast to the trend for UO_2. Consequently, the high thermal conductivity of U_3Si_2 can effectively lower fuel center line temperature, particularly at accident scenarios where fuels operate at higher temperatures than normal operating temperatures. The superior thermal conductivity of U_3Si_2 is attributed to the electronic origin of thermal conductance. However, same as UO_2, the thermal conductivity of U_3Si_2 can be degraded during service by the presence of irradiation induced defects, and the information is necessary for engineering scale fuel performance modeling.

As the thermal transport in U_3Si_2 is via a different mechanism from that in UO_2, the effect of irradiation induced damage, particularly lattice defects and dispersed fission products, can be different from that in UO_2. Moreover, U and Si can form several compounds depending on the composition. During fuel operation, phase decomposition can occur owing to local change in fuel chemistry. Therefore, it is desired to develop a thermal conductivity model that can describe the thermal conductivities of U-Si compounds with the effect of irradiation damage. In FY16, we have focused on fresh fuels with different Si content.

Assuming that the thermal transport is dominated by electrical contribution, a thermal conductivity model has been developed for unirradiated U-Si compounds including U_3Si_2. In the model, the thermal conductivity of U-Si compounds is dependent on U (Si) content and temperature. The heat transport by phonons (lattice vibration) and the effect of crystal structure are assumed to be negligible. This assumption is supported by the nearly linear increasing conductivity over temperature, and the linearly decreasing electronic density of state (DOS) with respect to Si content in several compounds including U_3Si, U_3Si_2 and U_3Si_5. To construct the model, we used the experimentally measured data for U [26], Si[27], U_3Si_2 [28] and U_3Si_5 [29] for fitting, and those for U_3Si [30] and USi [31] as validation.

As shown in Fig.7, the model fits well to the experimental data for U, Si, U_3Si2 and U_3Si_5. More encouragingly, it predicts well the thermal conductivity of U_3Si over the entire temperature range, which has not been used for fitting. For USi, the mode prediction agrees well with experimental measurements at low temperatures, and the discrepancy increases with elevating temperature. It has been suspected that the USi sample used in the experiments could possibly be non-stoichiometric, $U_{34}Si_{34.5}$ instead of USi [31]. Therefore, actual sample may contain some lattice defects and extra scattering should be considered which brings the model prediction down (dash green curve in Fig.7) and much closer to the experimental results. The good agreement between the model and experimental data suggests that the model based on Si concentration (thus impurity scattering) is suitable to describe thermal conductivity of unirradiated U-Si compounds, and suggests a promising way of treating irradiation induced damage in the future.

For more details of the model please refer to a separated report [32], where good agreement has also been reached between the model prediction and the result derived from irradiated U_3Si. The model has been implemented in the engineering scale fuel performance code BISON and is being implemented into MARMOT. The progress made in FY16 marks a inspiring starting point for the development of a thermal conductivity model including the effect of radiation damage. In FY17, the model will be extended to considering the effect of lattice defects, possibly based on electric resistivity. The effect of gas bubbles may also be considered by using MARMOT simulations.

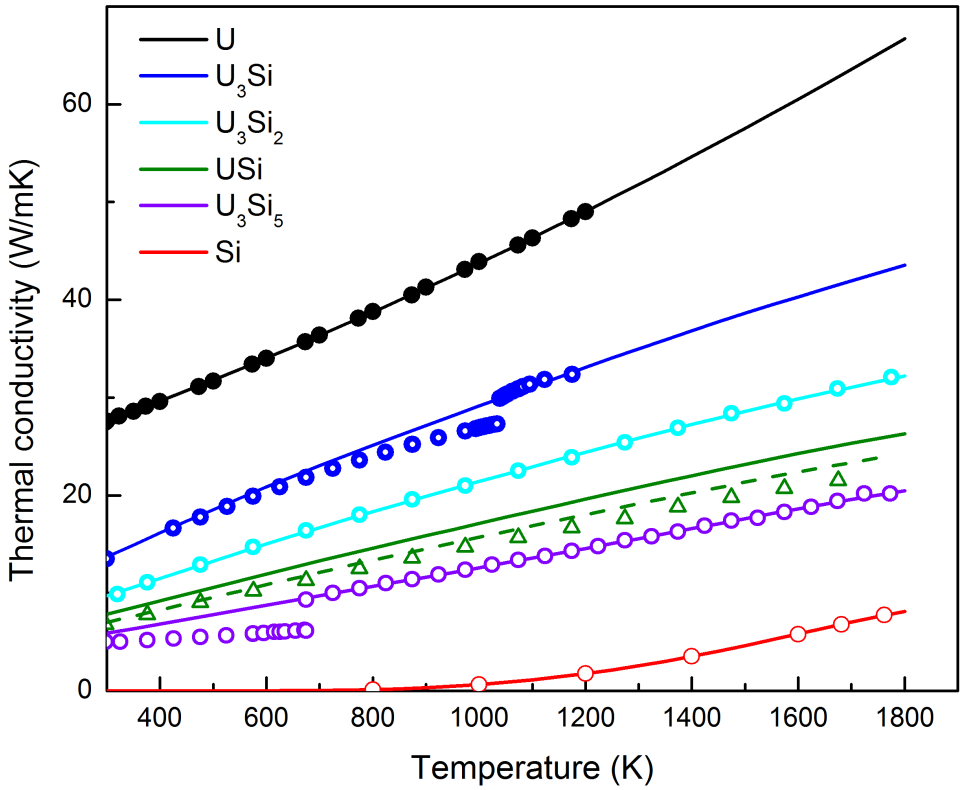

Figure 7: Thermal conductivities of U, U_3Si, U_3Si_2, USi, U_3Si_5 and Si as functions of temperature. The solid curves are the model predictions, and the symbols are experimental data. For Si only electrical contribution is plotted here. The dash green curve is corrected from solid green curve by including effect of lattice defects.

6 Lattice kinetic Monte-Carlo model development for FeCrAl cladding

6.1 Introduction

Fe-Cr-Al alloys with high Cr content (10-25wt%) and up to 5wt% Al have been recently proposed as candidate ATF cladding materials due to their excellent resistance to water corrosion (oxidation), and consequent reduction of heat and hydrogen generation during severe accidents [33]. The good corrosion resistance originates from the high Cr concentration and the protective Al oxide layer formed at the surface. Under neutron irradiation, the corrosion resistance of Fe-Cr-Al alloys can be degraded due to the precipitation of Cr-rich α' phase, which will deplete the Cr content in the matrix. α' precipitates can also hinder dislocation motion, leading to hardening and embrittlement. Note that, at the cladding operating temperature ($\sim$300-400°C), the precipitation process can be drastically accelerated under neutron irradiation due to radiation-enhanced-diffusion. While the irradiation effects have been extensively studied for Fe-Cr alloys, it is not clear how Al addition will change the α' precipitation, calling for mechanistic understanding from both modeling and experimental sides. The modeling efforts along this direction are summarized in this section.

6.2 Review of Kinetic Monte Carlo Modeling of Fe-X Alloys

In the past few decades, several kinetic Monte Carlo (KMC) simulations of have been performed to study the kinetics of coherent precipitation of solute elements (Cu and Cr) in bcc Fe under both thermal aging and irradiation conditions [34, 35, 36, 37, 38, 39]. In this report, only the thermal aging condition will be considered due to its relative simplicity. All previous simulations rely on the rejection-free residence time algorithm and transition state theory to model vacancy diffusion. For a bcc lattice, each vacancy has eight nearest neighbor sites to jump to, with the jump rate given by:

$$\Gamma_{X\to V} = \nu_X \exp\left(-\frac{E^{mig}_{X\to V}}{k_B T}\right) \tag{21}$$

where ν_X is the attempt frequency of the atom X jumping towards the vacancy, $E^{mig}_{X\to V}$ is the migration barrier of the X$\to$V jump, and k_B is Boltzmann's constant. Out of all possible eight jump events, one is selected by a random number and the average residence time is given by:

$$t_{MC} = \left(\sum_{i=1}^{8} \Gamma_i\right)^{-1} \tag{22}$$

Since the vacancy concentration in KMC simulations (c_V^{sim}) can be significantly greater than the thermal equilibrium vacancy concentration (c_V^{eq}), the physical time is advanced by:

$$t = t_{MC}\left(\frac{c_V^{sim}}{c_V^{eq}}\right) \tag{23}$$

The most important ingredient of a KMC model is the determination of local environment dependent vacancy migration barrier. According to the cut bond model (CBM) widely used in the literature [34, 35, 36, 37], $E^{mig}_{X\to V}$ can be estimated as follows:

$$E^{mig}_{X\to V} = e^{sp}_X - \sum_{i\in 1nn(X)} \varepsilon^{1nn}_{X-i} - \sum_{i\in 2nn(X)} \varepsilon^{2nn}_{X-i} - \sum_{i\in 1nn(V), i\neq X} \varepsilon^{1nn}_{V-i} - \sum_{i\in 2nn(V)} \varepsilon^{2nn}_{V-i} \tag{24}$$

where ε_{i-j} is the energy of a first nearest neighbor (1nn) or second nearest neighbor (2nn) i-j bond. e^{sp}_X is the energy of X atom at the saddle point (sp) position, which can be either assumed to be a constant [34, 35], or be calculated as $e^{sp}_X = \sum_i \varepsilon^{sp}_{X-i}$ [36, 37]. Here the summation goes over the six nearest neighbors of the X atom at the saddle point position.

An alternative form of the cut bond model (CBM2) has also been proposed [39], according to which:

$$E^{mig}_{X\to V} = e^{sp}_X + \sum_{i\in 1nn(X)} \varepsilon^{1nn}_{V-i} + \sum_{i\in 2nn(X)} \varepsilon^{2nn}_{V-i} - \sum_{i\in 1nn(X)} \varepsilon^{1nn}_{X-i} - \sum_{i\in 2nn(X)} \varepsilon^{2nn}_{X-i} \tag{25}$$

The new CBM2 model considers the fact that the migrating atom X will leave a vacancy behind once it moves to the saddle point position. This is in contrast to the original CBM model, which assumes that the bonds associated with the migrating X atom and vacancy are all broken.
Finally, the migration barrier can be estimated from the final and initial system energy (FISE) [39] as:

$$E^{mig}_{X\to V} = E^{mig}_X + \Delta E/2 \tag{26}$$

where $E^{mig}_{X\to V}$ is the migration barrier for $X \to V$ jump in pure bcc Fe. $\Delta E = E_f - E_i$ is the energy difference before and after the vacancy jump, which can either directly calculated from an empirical interatomic potential, or can be estimated using the pair interaction model as:

$$\begin{aligned}\Delta E = &\sum_{i\in 1nn(X), i\neq V} \varepsilon^{1nn}_{V-i} + \sum_{i\in 2nn(X)} \varepsilon^{2nn}_{V-i} + \sum_{i\in 1nn(V), i\neq X} \varepsilon^{1nn}_{X-i} + \sum_{i\in 2nn(V)} \varepsilon^{2nn}_{X-i} \\ &- \sum_{i\in 1nn(X), i\neq V} \varepsilon^{1nn}_{X-i} - \sum_{i\in 2nn(X)} \varepsilon^{2nn}_{X-i} - \sum_{i\in 1nn(V), i\neq X} \varepsilon^{1nn}_{V-i} - \sum_{i\in 2nn(V)} \varepsilon^{2nn}_{V-i}\end{aligned} \tag{27}$$

In this formulation, the 1nn X-V bond is intentionally neglected in the summations since it exists in both the initial and final states and will therefore cancel out.

In practice, the bond energies ε^{1nn}_{i-j} and ε^{2nn}_{V-i} are usually fitted to experimental or theoretical data such as the cohesive energies and vacancy formation energies of pure elements, the solution energies of solutes in bcc Fe, the mixing energies of random Fe-X alloys, the solute-solute and solute-vacancy binding energies, often with the additional assumption that $\varepsilon^{2nn}_{i-j} = \frac{1}{2}\varepsilon^{2nn}_{i-j}$ [35, 37]. The saddle point energy e^{sp}_X can be fitted to the migration barriers for self-diffusion and impurity-diffusion in pure bcc Fe via the vacancy mechanism.

6.3 Progress of KMC Modeling of Fe-Cr and Fe-Al Alloys

In this work, the FISE model is employed to model binary Fe-Cr and Fe-Al alloys. For parameterization of the bond energies, ab initio calculations based on density functional theory (DFT), as implemented in the Vienna ab initio simulation package (VASP) code [40], have been performed to directly obtain the total energies of the initial and final states of a vacancy jump in a random Fe-X (X=Cr, Al) alloy. All calculations are performed within the generalized gradient approximation (GGA) with the Perdew-Burke-Ernzerhof (PBE) exchange-correlation function [41]. The plane

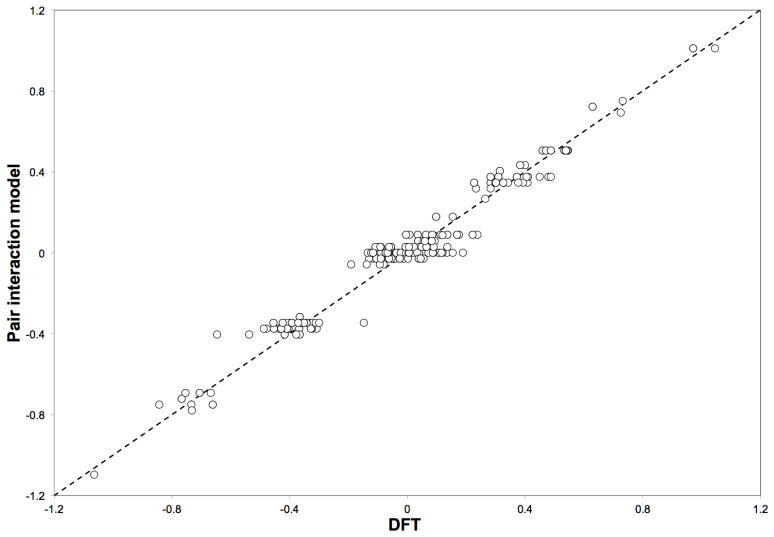

Figure 8: Comparison between DFT calculated and model predicted ΔE values (in eV) in bcc Fe_8Al_1 alloy.

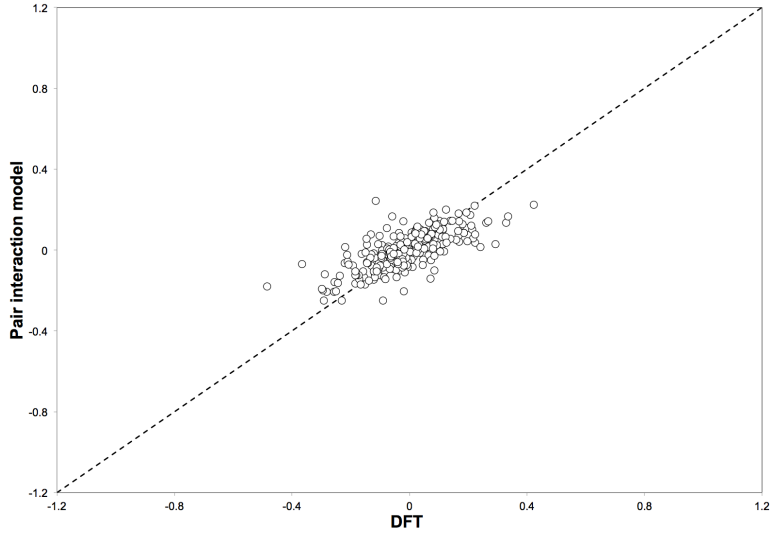

Figure 9: Comparison between DFT calculated and model predicted ΔE values (in eV) in bcc Fe_2Cr_1 alloy.

wave cutoff energy is set at 350 eV. The k-point meshes for Brillouin zone sampling are constructed using the MonkhorstPack scheme and the total number of k-points times the total number of atoms per unit cell was at least 5000 for all structures. The migration barriers for vacancy jumps are obtained from climbing image nudged elastic band (CI-NEB) calculations [42]. All calculations are spin-polarized to take into account the magnetic nature of Fe and Cr.

Figures 8 and 9 show the comparisons between DFT calculated and model predicted ΔE values for bcc Fe-Al and Fe-Cr alloys, respectively. Equation 27 is used in the fitting, which considers composition-independent pair interactions up to the 2nn. The average fitting error is 0.07 eV for Fe-Al and 0.09 eV for Fe-Cr. Our test calculations show that extending the pair interaction range to third-nearest neighbor does not improve the fitting.

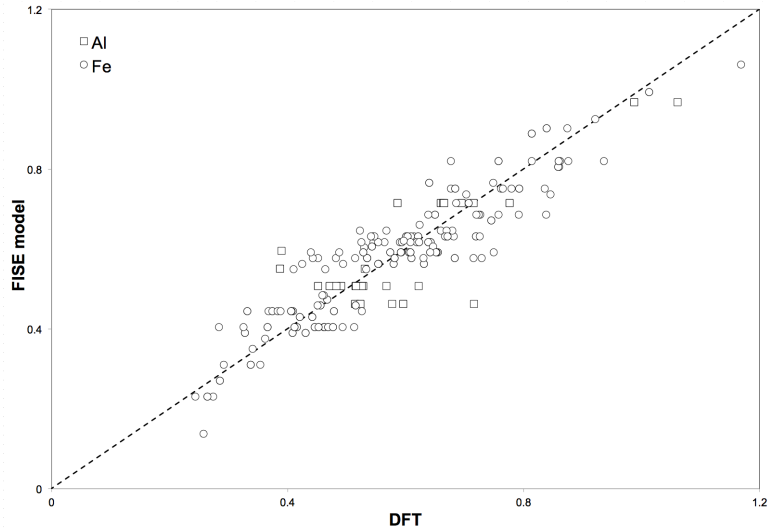

Figure 10: Comparison between DFT calculated and model predicted migration barriers (in eV) for vacancy jumps in bcc Fe_8Al_1 alloy.

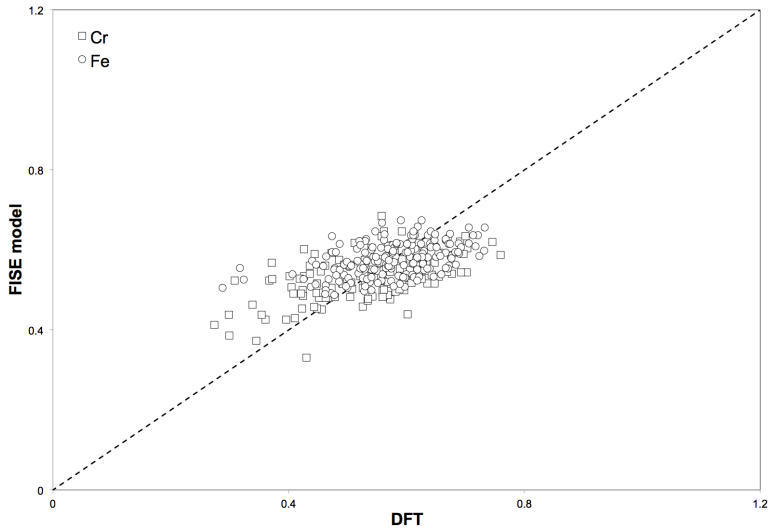

Figure 11: Comparison between DFT calculated and model predicted migration barriers (in eV) for vacancy jumps in bcc Fe_2Cr_1 alloy.

From the model calculated ΔE, the migration barriers for vacany jump into a Fe or X atom can be estimated using Equation 26. Figures 10 and 11 show the comparisons between NEB calculated and FISE model predicted migration barriers in Fe-Al and Fe-Cr alloys. The average fitting error is 0.07 eV for Fe-Al and 0.08 eV for Fe-Cr. The results show that, unlike bcc Fe-Cr, the vacancy migration barriers in bcc Fe-Al are strongly dependent on local environments with values ranging from less than 0.2 eV to more than 1 eV, which is due to the strong binding between Al atom and vacancy.

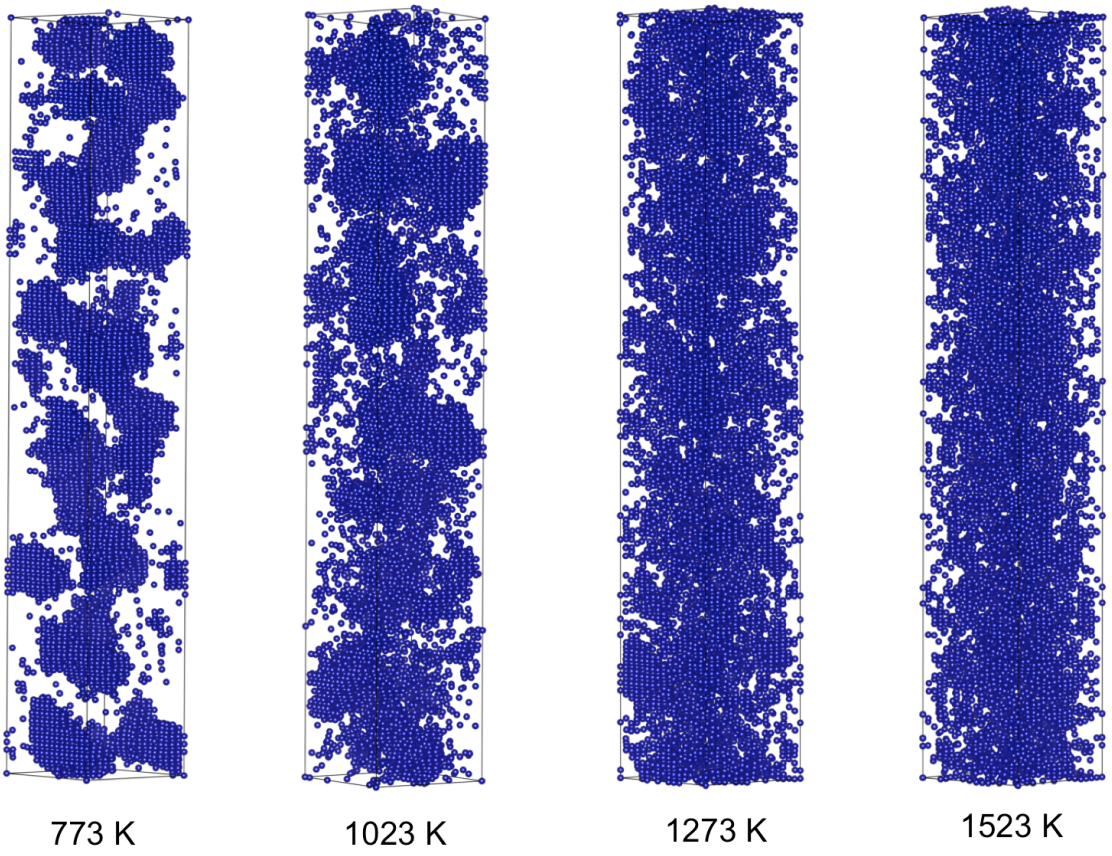

Figure 12: KMC simulation of Cr precipitation in bcc Fe-20Cr alloy. Only Cr atoms are shown.

6.4 Simulation results

With the set of parameters for KMC modeling developed in this work, the precipitation of α' phase from bcc Fe-Cr alloys under thermal aging have been simulated at various temperatures and the results are shown in Figure 12. Precipitation of Cr from the solid solution is observed at 773 K and 1023 K, but not at 1273 K and 1523 K. From the experimental Fe-Cr phase diagram [43], the critical temperature for α' precipitation in a Fe-20Cr alloy is about 900 K. The present KMC model slightly overestimates the critical temperature, which is possibly due to the neglect to vibrational and magnetic contributions to the free energy. In contrast to Fe-Cr system, Fe-Al alloys do not show any phase separation, as shown in Figure 13. This is also consistent with the fact that Fe-Al is an ordering-type system.

6.5 Summary

In this work, a new scheme is developed that allows parameterization of a KMC model based on inputs from DFT calculations of random alloys. Two types of DFT data, i.e. total energy change associated with a nearest-neighbor vacancy jump and the migration barrier, are used in the fitting. We demonstrate the usefulness of this new scheme by applying it to parameterize KMC models of Fe-Cr and Fe-Al binary systems. Extension of our approach to model the coherent participation kinetics of Cr in Fe-Cr-Al cladding under thermal aging conditions should be straightforward.

While the present KMC model can capture the major features of the Fe-Cr and Fe-Al systems,

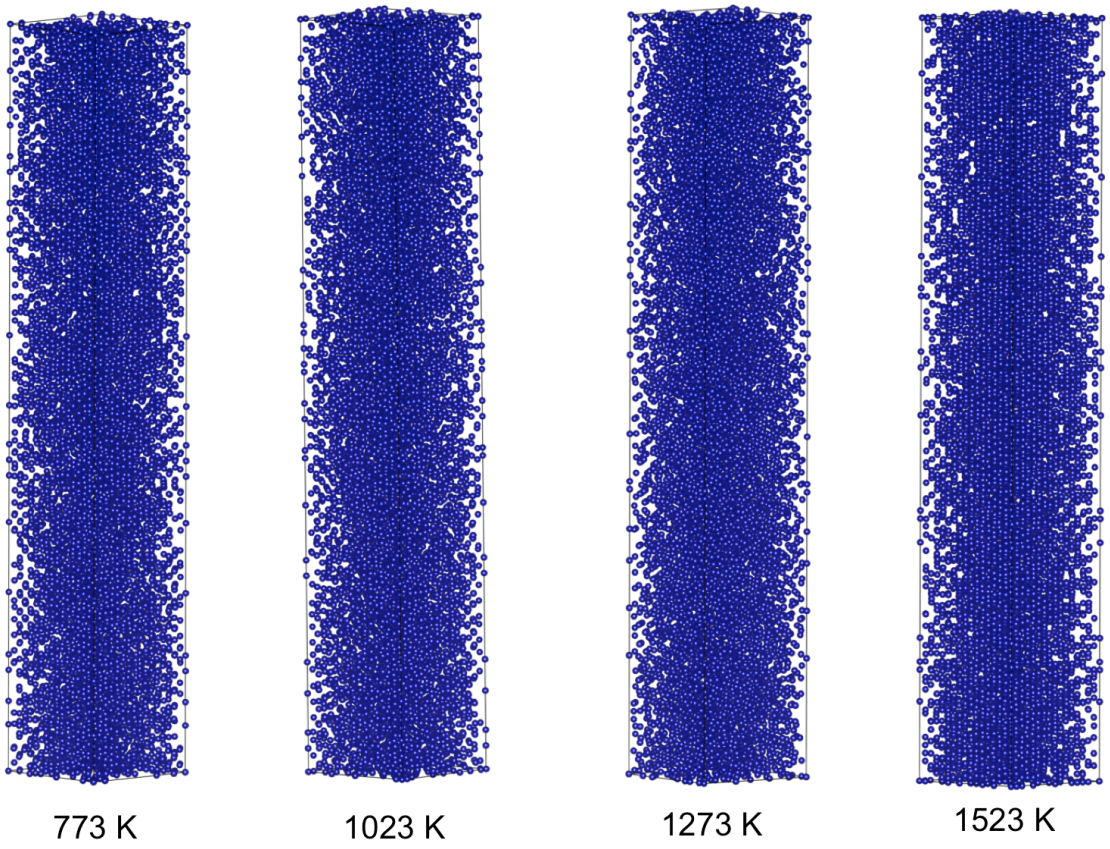

Figure 13: KMC simulation of bcc Fe-10Al alloy. Only Al atoms are shown.

there exist several limitations. One limitation is that Cr-Cr interaction remains attractive even in the dilute solid solution phase. To address this issue, we will continue to develop a composition-dependent bond energy model to account for the ordering tendency in dilute Fe-Cr alloys. Another limitation is due to the neglecting of magnetic and vibrational contributions to the free energy, which will be considered in our future study. Finally, the adoption of a second-nearest neighbor pair interaction model may limit the accuracy of our model. This may be improved by using more accurate cluster expansion method to better describe the energetic of small precipitates.

7 Summary

In summary, in FY16 lower-length-scale efforts have been made to develop atomic scale and mesoscale tools and develop engineering scale materials models for U_3Si_2 fuel and FeCrAl cladding in the below areas:

1) Two interatomic potentials, one Tersoff type and one modified embedded-atom-method type, have been developed for U_3Si_2 with the focus on phase stability and elasticity. Extensions of the potentials have been made to include Xe for the purpose of simulating fission gas. The potential may also been used to describe other U-Si compounds such as U_3Si. These potentials will be utilized to calculate the interfacial energies, defect formation energies and their interactions with fission gas and interfaces, and to simulate defect production in U_3Si_2, for the purposes of improving fundamental understanding and providing input for upper scale models.

2) A Kim-Kim-Suzuki (KKS) phase field model has been developed in MARMOT for the phase stability of U-Si compounds including U_3Si_2, USi, U_3Si, and liquid phases. Free energies from the CALPHAD database have been taken and implemented. The model correctly reproduced three-phase coexistence in a U_3Si_2-liquid-USi system at the eutectic temperature, solidification of a three-phase mixture below the eutectic temperature, and complete melting of a three-phase mixture above the eutectic temperature. Further details are available in Ref. [23]. This model, with some more parameters to be provided from atomistic calculations, will be used to investigate phase evolution during fuel operation and possible fuel melting at accident scenarios.

3) A phase field model has been developed in MARMOT for gas bubble swelling. A unique feature of this model is that it can describe the formation of voids and bubbles when the global concentration is dilute but well above the thermal equilibrium. Currently, material parameters are being collected to enable gas bubble formation simulations in U_3Si_2. In FY17, this model will be used to estimate gas bubble swelling in U_3Si_2 fuel. Comparison of gas bubble swelling in U_3Si_2 and UO_2 will also be compared.

4) A thermal conductivity model for unirradiated U-Si compounds has been developed and implemented into BISON. This model describes the thermal conductivity of a certain U-Si compounds as a function of Si content and temperature. It is fitted using experimental data for U, U_3Si_2, U_3Si_5 and Si, and shows good predictivity for U_3Si and USi. In FY17, the model will be extended to include degradation caused in lattice defects and will be used in MARMOT simulations to assess the effect of gas bubbles.

5) A lattice kinetic Monte Carlo model has been developed for Fe-Cr and Fe-Al binary alloys by fitting the bond energies using density functional theory calculations. In the fitting, an arbitrary assumption, which depicts the second nearest neighbor interaction to be fractional of that of the first and is widely used for convenience in previous models, is abandoned for better accuracy. In FY17, the model will be improved by including composition-dependent bond energies for Fe-Cr, and extended for Fe-Cr-Al ternary systems. The ternary system will be used to study precipitation in FeCrAl alloys under thermal aging and neutron irradiation.

While improving our understanding on these two new fuel concept, the results are also expected to feature multiple journal publications and conference presentations.

8 References

1. S Bragg-Sitton. Development of advanced accident-tolerant fuels for commercial lwrs. *Nuclear News*, page 83, March 2014.

2. K.A. Terrani, S.J. Zinkle, and L.L. Snead. Code verification by the method of manufactured solutions. *Journal of Nuclear Materials*, 448:420, 2014.

3. M. Noordhoek, T. Besman, D.A. Andersson, S. Middlesburgh, and A. Chernatynskiy. Phase equilibria in the u-si system from first-principles calculations. *J. Nucl. Mater.*, 479:216–223, 2016.

4. J. Yu, Y. Zhang, and J. Hales. Milestone report on md potential development for uranium silicide. Technical report, Idaho National Laboratory, 2016.

5. J. Yu, Y. Zhang, and J. Hales. Development of molecular dynamics potential for uranium silicide fuels. In *Proceedings of Top Fuel 2016. Boise, USA*, 2016.

6. M. Daw and M. Baskes. Embedded-atom method - derivation and application to impurities, surfaces, and other defects in metals. *Phys. Rev. B*, 29:6443, 1984.

7. M. Daw, S. Foiles, and M. Baskes. The embedded-atom method: a review of theory and applications. *Mat. Sci. Rep.*, 9:251–310, 1993.

8. M. Daw and M. Baskes. Semiempirical, quantum mechanical calculation of hydrogen embrittlement in metals. *Phys. Rev. Lett.*, 50:1285, 1983.

9. P. Olsson. Semi-empirical atomistic study of point defect properties in bcc transition metals. *Comp. Mat. Sci.*, 47:135, 2009.

10. D. Belaschenko and D. Smirnova. Modeling the molecular dynamics of liquid metals at high pressures: Liquid potassium. *Russ. J. Phys. Chem.*, 85:1908, 2011.

11. X. Liu, H. Liu, J. Dong, and X. Xie. Molecular dynamics simulation on phosphorus behavior at ni grain boundary. *Scripta Materialia*, 42:189, 1999.

12. M. Chassange, M. Legros, and D. Rodney. Atomic-scale simulation of screw dislocation/coherent twin boundary interaction in al, au, cu and ni. *Acta mater.*, 59:1456, 2011.

13. G. Li, Q. Wang, D. Li, and J. He. Size and composition effects on the melting of bimetallic cu?ni clusters studied via molecular dynamics simulation. *Mater. Chem. Phys.*, 114:746, 2009.

14. I. Vatne, E. Ostby, C. Thaulow, and D. Farkas. Multiscale simulations of mixed-mode fracture in bcc-fe. *Mat. Sci. Eng. A*, 528:5122, 2011.

15. J. Rose, J. Smith, F. Guinea, and J. Ferrante. Universal features of the equation of state of metals. *Phys. Rev. B*, 29:2963, 1984.

16. M. Baskes. Modified embedded-atom potentials for cubic materials and impurities. *Phys. Rev. B*, 46:2727, 1992.

17. M. Baskes. Second nearest-neighbor modified embedded-atom-method potential. *Phys. Rev. B*, 62:15532, 2000.

18. M. Baskes. Application of the embedded-atom method to covalent materials: A semiempirical potential for silicon. *Phys. Rev. Lett.*, 59:2666, 1987.

19. M. Baskes, J. Nelson, and A. Wright. Semiempirical modified embedded-atom potentials for silicon and germanium. *Phys. Rev. B*, 40:6085, 1989.

20. R. Ravelo and M. Baskes. Equilibrium and thermodynamic properties of grey, white, and liquid tin. *Phys. Rev. Lett.*, 79:2482, 1997.

21. A. Moore, B. Beeler, C. Deo, M. Baskes, and M. Okuniewski. Atomistic modeling of high temperature uranium-zirconium alloy structure and thermodynamics. *J. Nucl. Mater.*, 467:802, 2015.

22. S J Plimpton. Fast parallel algorithms for short-range molecular dynamics. *J. Comp. Phys.*, 117:1–19, 1995.

23. L. K. Aagesen and D. Schwen. MARMOT phase-field model for the U-Si system. Technical Report INL/EXT-16-XXXXX, 2016.

24. J. Rest and Hofman G. Dynamics of irradiation-induced grain subdivision and swelling in u_3si_2 and uo_2 fuels. *Journal of Nuclear Materials*, 210:187, 1994.

25. M. Plapp. Unified derivation of phase-field models for alloy solidification from a grand-potential functional. *Physical Review E*, 84:031601, 2011.

26. C. Y. Ho, M. W. Ackerman, K. Y. Wu, S. G. Oh, and T. N. Havil. Thermal conductivity of ten selected binary alloy systems. *Journal of Physical and Chemical Reference Data*, 7:959, 1978.

27. C. J. Glassbrenner and G. A. Slack. Thermal conductivity of silicon and germanium from 3k to the melting point. *Physical Review*, 134:A1059, 1964.

28. J. T. White, A. T. Nelson, J. T. Dunwoody, D. D. Byler, D. J. Safarik, and K. McClellan. Thermophysical properties of u3si2 to 1773 k. *Journal of Nuclear Materials*, 464:275, 2015.

29. J. T. White, A. T. Nelson, D. D. Byler, D. J. Safarik, J. T. Dunwoody, and K. J. McClellan. Thermophysical properties of u3si to 1150 k. *Journal of Nuclear Materials*, 452:304, 2015.

30. J. T. White, A. T. Nelson, D. D. Byler, J. A. Valdez, and K. J. McClellan. Thermophysical properties of u3si to 1150 k. *Journal of Nuclear Materials*, 452:304, 2014.

31. J. T. White, A. T. Nelson, J. T. Dunwoody, D. D. Byler, and K. J. McClellan. Thermophysical properties of usi to 1773 k, journal of nuclear materials. *Journal of Nuclear Materials*, 471:129, 2016.

32. Y Zhang and D Andersson. A thermal conductivity model for u-si compounds. Technical report, Idaho National Laboratory, 2016.

33. Y Zhang, D Schwen, C Jiang, and E Martinez. Literature review report on atomistic modeling tools for fecral alloys. Technical report, Idaho National Laboratory, 2015.

34. F Soisson, A Barbu, and G Martin. Monte carlo simulations of copper precipitation in dilute iron-copper alloys during thermal ageing and under electron irradiation. *Acta Materialia*, 44:3789–3800, 1996.

35. S Schmauder and P Binkele. Atomistic computer simulation of the formation of cu-precipitates in steels. *Computational Materals Science*, 24:42–53, 2002.

36. F Soisson and CC Fu. Cu-precipitation kinetics in alpha-fe from atomistic simulations: Vacancy-trapping effects and cu-cluster mobility. *Physical Review B*, 76:214102, 2007.

37. E Martinez, O Senninger, F Soisson, and CC Fu. Decomposition kinetics of fe-cr solid solutions during thermal aging. *Physical Review B*, 86:214109, 2012.

38. F Soisson and T Jourdan. Radiation-accelerated precipitation in fe-cr alloys. *Acta Materialia*, 103:870–881, 2016.

39. E Vincent, CS Becquart, C Pareige, P Pareige, and C Domain. Precipitation of the fecu system: A criticle review of atomic kinetic monte carlo simulations. *Journal of Nuclear Materials*, 373:387–401, 2008.

40. G Kresse and J Furthmuller. Efficient iterative schemes for ab initio total-energy calculations using a plane-wave basis set. *Physical Review B*, 54:11169–11186, 1996.

41. JP Perdew, K Burke, and M Ernzerhof. Generalized gradient approximation made simple. *Physical Review Letters*, 77:3865–3868, 1996.

42. G Henkelman and H Jonsson. A climbing image nudged elastic band method for finding saddle points and minimum energy paths. *Journal of Chemical Physics*, 113:9901–9904, 2000.

43. W Xiong, P Hedstrom, M Selleby, J Odqvist, M Thuvander, and Chen Q. An improved thermodynamic modeling of the fecr system down to zero kelvin coupled with key experiments. *CALPHAD*, 35:355–366, 2011.